Marangoni effect on the impact of droplets onto a liquid-gas interface

Feifei Jia,[1] Kai Sun,[1,*] Peng Zhang,[2] Cuicui Yin,[1] and Tianyou Wang[1]
[1]*State Key Laboratory of Engines, Tianjin University, Tianjin 300072, China*
[2]*Department of Mechanical Engineering, The Hong Kong Polytechnic University, Hong Kong 999077, China*

(Received 3 December 2019; accepted 6 July 2020; published 27 July 2020)

The impact dynamics and internal mixing of a droplet onto a liquid-gas interface of lower surface tension was studied both experimentally and numerically, with both the *Ohnesorge* number (Oh) and the *Bond* number (Bo) being fixed. Compared to the droplet impact onto a pool of identical liquid, the interfacial Marangoni flow entrains abundant fluid upward and hence induces an additional jet breakup during crater formation (the first breakup), and it facilitates the emergence of the Rayleigh jet breakup (the second breakup) during crater restoration and enhances the vortical mixing beneath the liquid surface. Specifically, with the increase of the impact inertia, the first breakup manifests a nonmonotonic trend of "absence-presence-absence." The former transition of "absence-presence" at a low droplet-based *Weber* number (We_d) is caused by the shortened path of the Marangoni flow on the faster-growing liquid bridge, and the later transition of "presence-absence" at a high We_d is resulted from the reduced displacement velocity of the pool fluid on the expanding crater surface. The second breakup corresponds to the Rayleigh jet breakup without surface tension difference and occurs monotonically beyond a certain We_d. Due to the relatively short displacement time of the Marangoni flow on the crater surface compared to the time for crater formation, the critical condition for the emergence of the second jet breakup could be described by the critical reservoir-fluid-based We number (We_r). The critical We_r contains two parts: the Bo-dependent critical We_{r0} without surface tension difference, and the increased viscous dissipation from the wrap-up motion of the Marangoni flow. Furthermore, capillary waves are also induced by the Marangoni flow during crater restoration, and the accompanied vorticity generation causes the mixing pattern to exhibit multiple vortex rings and even a clawlike structure, which is substantially enhanced compared to the vortical mixing without surface tension difference.

DOI: 10.1103/PhysRevFluids.5.073605

I. INTRODUCTION

The impact of droplets onto a liquid surface occurs universally in a number of natural and industrial processes including precipitation [1], spray atomization in engines [2], spray cooling [3], *etc.* For decades, most studies have focused on the droplet impact of an identical liquid, and various impact outcomes have been reported, including bouncing, complete coalescence, partial coalescence, jet breakup (singular jet and cavity jet), and splashing [4–8]. Beneath the liquid surface, jetlike mixing was also identified [9,10].

With the rapid development of novel technologies such as microfluidic devices [11,12], material synthesis [13,14], and hypergolic propulsion systems [15,16], the impact of droplets onto a liquid surface of unlike physical properties has attracted increasing attentions due to its practical relevance. Physically, the droplet impact process is synergistically controlled by the impact inertia, surface

*Author to whom correspondence should be addressed: sunkai@tju.edu.cn

tension, and viscous dissipation, therefore the disparity in either the viscosity or the surface tension between the droplet and the pool could significantly affect the impact dynamics and the internal mixing. In the presence of viscosity disparity, the internal flow would be passively modulated by the viscous dissipation, resulting in vortex-induced buckling of the droplet [17], bursting of microbubbles during the air layer rupture [18,19], as well as distinct morphology of the splashing corolla [20].

In contrast, the surface tension difference between the droplet and the reservoir fluid may also arise from differences in their composition or temperature. It induces tangential stress on the liquid-gas interface upon coalescence and therefore generates additional interfacial Marangoni flow to interact with the complex bulk flow. In this regard, Blanchette *et al.* [21] experimentally identified the emergence of "partial coalescence" when the surface tension of the reservoir fluid, σ_r, is substantially smaller compared to that of the droplet fluid, σ_d. Sun *et al.* [22] further revealed that the critical condition for such "partial coalescence" depends on the ratio of two characteristic timescales of the vertical collapse and the horizontal collapse during droplet deformation. Martin and Blanchette [23] numerically showed that a moderate surface tension difference induced by surfactant also facilitates complete coalescence. Kim *et al.* [24] experimentally found that, when an alcohol droplet is placed on a water reservoir of infinite miscibility, a static "liquid lens" is formed in the middle without immediately spreading and mixing, and a quasisteady, outward Marangoni flow is established along the rim of the "liquid lens." Furthermore, the coalescence of two droplets of different surface tensions was found to result in encapsulation of the droplet with higher surface tension into the other droplet with lower surface tension, and enhanced mixing was also identified with such "wrapping" motion [25].

The above studies have identified the significant influence of Marangoni flow on the droplet coalescence with a near-zero impact velocity. When the impact velocity is non-negligible, which occurs much more frequently in reality, the synergistic effect of impact inertia, surface tension, viscous force, and Marangoni flow on the droplet impact process would be even more complicated, and it still remains to be explored. In the present study, therefore, we aim to experimentally and numerically investigate the Marangoni effect on the impact of a droplet onto a liquid pool. Only the scenario of $\sigma_d > \sigma_r$ is considered, as the Marangoni-flow-driven "wrapping" motion imposes a counter action to the impact-inertia-driven "spreading" motion. In the following, the experimental and numerical methods, results and discussion, and concluding remarks will be sequentially presented in Secs. II to IV.

II. EXPERIMENTAL AND NUMERICAL METHODS

A. Experimental setup

The experimental setup is schematically shown in Fig. 1. Deionized water droplets were generated from a syringe pump (Harvard Apparatus, Pump 11 elite Pico plus) and freely fell onto a liquid pool of ethanol or ethanol-water solution by gravity. A high-speed camera (Photron SA 1.1) was used to record the impact process twice from both front view and aerial views, with a shooting speed of 5400 frames per second and a resolution of 1024×1024 pixels. An LED lamp and a diffuser were also used to provide even light for imaging. The droplet diameter D_0 was controlled by the size of the needle, and exactly measured by counting the number of pixels on the recorded images. The impact velocity U was tuned by the falling height of the droplet, and exactly determined through the displacement of the droplet center (an average coordinate of the lower and upper interfaces) within the last two frames prior to impact. The surface tension of the reservoir fluid σ_r was varied by the ethanol concentration. The size of the liquid reservoir ($4 \times 4 \times 4\,\mathrm{cm}^3$) was large enough compared to the droplet to eliminate possible boundary effects. During the experiment, room temperature was 24 °C and humidity was 28.6%.

According to dimensional analysis, eight nondimensional parameters are required to describe the flow similarity of the present problem, including the nondimensional surface tension difference

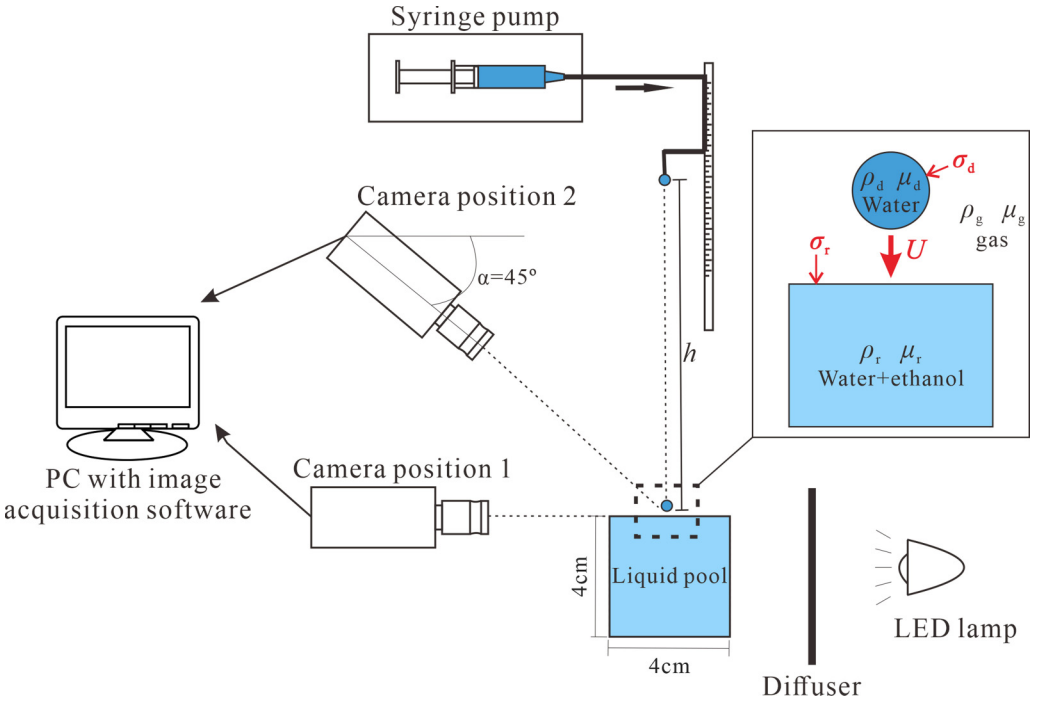

FIG. 1. Schematic of the experimental setup.

$1-\sigma^* = (\sigma_d - \sigma_r)/\sigma_d$, the droplet-based *Weber* number $We_d = \rho_d D_0 U^2/\sigma_d$, the *Ohnesorge* number $Oh = \mu_d/\sqrt{\rho_d D_0 \sigma_d}$, the *Bond* number $Bo = (\rho_d - \rho_g) g D_0^2/\sigma_d$, the droplet-gas density ratio ρ_d/ρ_g, the droplet-gas viscosity ratio μ_d/μ_g, the reservoir-droplet density ratio ρ_r/ρ_d, and the reservoir-droplet viscosity ratio μ_r/μ_d. In the present water-ethanol system, ρ_r/ρ_d is close to unity, and we neglected the density disparity between the droplet and the reservoir fluid; μ_d/μ_g may vary in the range of 1.0–2.4, depending on the volume fraction of ethanol in the reservoir liquid, and we approximate this factor to be an increased effective Oh number in the following discussion; both ρ_d/ρ_g and μ_d/μ_g are large enough to eliminate inertia and viscous effects from the ambient gas. Furthermore, the droplet diameter was fixed at approximately 2.4 mm, and hence Oh and Bo are close to 0.0022 and 0.75, respectively. Therefore, among the eight nondimensional parameters, $1-\sigma^*$ and We_d are varied as two controlling parameters in the present study. The ranges of the parameters are summarized in Table I, and an error analysis of the nondimensional parameters is

TABLE I. Nondimensional parameters in the experiment.

Parameter	Value or range
Nondimensional surface tension difference, $1-\sigma^* = (\sigma_d - \sigma_r)/\sigma_d$	0.0–0.7
Droplet-based *Weber* number, $We_d = \rho_d U^2 D_0/\sigma_d$	5–300
Ohnesorge number, $Oh = \mu_d/\sqrt{\rho_d \sigma_d D_0}$	0.0022
Bond number, $Bo = (\rho_d - \rho_g) g D_0^2/\sigma_d$	0.75
Droplet-gas density ratio, ρ_d/ρ_g	1000
Droplet-gas viscosity ratio, μ_d/μ_g	55
Reservoir-droplet density ratio, ρ_r/ρ_d	0.8–1.0
Reservoir-droplet viscosity ratio, μ_r/μ_d	1.0–2.4

given in Appendix A. It is also noted that, in the experiment, although the falling droplets are still subject to avoidable oscillation upon impact for $We_d < 30$, such effect is negligible on the following results according to our test.

B. Numerical method

In view of the fact that the normal impact of a droplet onto a liquid pool is symmetric with respect to the axis across the center of the droplet and normal to the pool interface, we performed numerical simulation in an axisymmetric domain, where the bottom of the reservoir is a rigid wall and the other two sides are open boundaries. The liquid pool and the ambient gas are initially stationary, while the droplet is placed above the pool with a short distance of $1/8D_0$ and given a downward velocity U (the acceleration of the droplet by gravity prior to impact is negligible). The droplet and the pool are given different surface tensions, while their differences in density and viscosity are neglected.

The phase-field method [26,27] is employed to model the interface dynamics. A composition C, which denotes the volume fraction of liquid in local fluid, is used to capture the interface between the liquid and the ambient gas. The evolution of C is governed by the *Cahn-Hilliard* equation:

$$\frac{\partial C}{\partial t} + \boldsymbol{u} \cdot \nabla C = M \nabla^2 \mu_C, \tag{1}$$

where $\boldsymbol{u}$ is the velocity, M is the interface mobility, and $\mu_C = \mu_0 - k\nabla^2 C = \partial E_0/\partial C - k\nabla^2 C$ is the chemical potential with E_0 being the bulk free energy and k the gradient factor. The bulk free energy takes a double-well function $E_0 = \beta C^2(1-C)^2$ and the chemical potential is given by $\mu_C = \beta(4C^3 - 6C^2 + 2C) - k\nabla^2 C$ [28]. For single-component two-phase flows, β and k are constants that determine the surface tension and the interface thickness by $\sigma = \sqrt{2k\beta}/6$ and $\xi = \sqrt{8k/\beta}$, respectively.

To capture the temporal and spatial variation in the local surface tension along the liquid-gas interface, another passive scalar C_1 is employed to capture the convective and diffusive transport of the lower surface tension fluid (i.e., the pool liquid):

$$\frac{\partial C_1}{\partial t} + \boldsymbol{u} \cdot \nabla C_1 = \nabla \cdot (D \nabla C_1) + \widetilde{C_1} M \nabla^2 \mu_C, \tag{2}$$

where D is the composition diffusivity and $\widetilde{C_1} = C_1/C$ denotes the proportion of pool fluid in local liquid. The second term on the right-hand side (RHS) of Eq. (2) describes the partial contribution of the pool liquid to the total Cahn-Hilliard diffusion of the liquid-gas interface.

In the simulation, to maintain a uniform interface thickness, β, k, and M in Eq. (1) are chosen to vary with the local surface tension by $k = k_0\sigma/\sigma_d$, $\beta = \beta_0\sigma/\sigma_d$, and $M = M_0\sigma_d/\sigma$, where the normalized local surface tension σ/σ_d is determined by $\widetilde{C_1}$ and takes the following fitting expression [21]:

$$\sigma/\sigma_d = 0.21551 e^{-0.03727\widetilde{C_1}} + 0.49521 e^{-0.29957\widetilde{C_1}} + 0.28761. \tag{3}$$

In addition to Eqs. (1) and (2), the continuity equation and the momentum equation for incompressible flows are also included:

$$\nabla \cdot \boldsymbol{u} = 0 \tag{4}$$

and

$$\rho\left[\frac{\partial \boldsymbol{u}}{\partial t} + \boldsymbol{u} \cdot \nabla \boldsymbol{u}\right] = -\nabla p + \nabla \cdot [\mu(\nabla \boldsymbol{u} + \nabla \boldsymbol{u}^T)] + \mu_C \nabla C + |\nabla C|^2 \nabla k - (\nabla k \cdot \nabla C)\nabla C + \rho g, \tag{5}$$

TABLE II. Simulation cases in the present study.

Case	We_d	$1-\sigma^*$	Oh	Fixed parameters
1	10	0.7	0.0022	
2	40	0.7	0.0022	
3	70	0.7	0.0022	Bo = 0.75
4	20	0.5	0.004	$\rho_d/\rho_g = 500$
5	90	0.5	0.004	$\mu_d/\mu_g = 50$
6	120	0.5	0.004	$\rho_r/\rho_d = 1$
7	10	0	0.0022	$\mu_r/\mu_d = 1$
8	40	0	0.0022	
9	70	0	0.0022	

where p is the pressure, μ is the dynamic viscosity, and g is the gravitational acceleration. On the RHS of Eq. (5), the third term represents surface tension, and the fourth and fifth terms represent the Marangoni stress in potential form.

Moreover, the local fluid density and dynamic viscosity are taken linear functions of C by

$$\rho = \rho_d C + \rho_g (1 - C), \tag{6}$$

and

$$\mu = C\mu_d + (1 - C)\mu_g. \tag{7}$$

In the present study, Eqs. (1), (4), and (5) are numerically solved by using the lattice Boltzmann method (LBM) [29], which has been developed to be an efficient flow solver for multiphase flows with high density ratios and viscosity ratios in recent years [30–35]. In the present LBM simulation, two distribution functions are used to recover Eqs. (1), (4), and (5) [28,31]. The multiple-relaxation-time collision operator [36] is adopted to improve the numerical stability, and the potential form of interfacial forces and the isotropic finite difference are employed to suppress the notorious spurious current to a relatively low level at realistic liquid-gas density ratios [31]. Detailed transformation from the macroscopic governing equations to the LBM evolution equations in an axisymmetric coordinate can be found in the authors' previous paper [37]. Furthermore, it is also noted that modeling the Marangoni flow is rather challenging within a finite interface thickness. As such, Eq. (2) is not included in the framework LBM but instead solved by using the finite difference method with the third-order Runge-Kutta method [38] for time discretization and the fifth-order weighted essentially nonoscillatory (WENO) scheme [39] for spatial discretization.

We also note that numerical simulation of the present problem is indeed not an easy task. To the authors' knowledge, similar scenarios with a large liquid-gas density ratio and a large surface tension difference have been rarely simulated in literature. Moreover, a few different length scales are involved in the present problem such as the droplet diameter, the impact crater diameter, the Marangoni-flow-induced shear layer beneath the interface, the diameters of the ejected satellite droplets, etc., which make the numerical simulation even more challenging. Therefore, the aim of the present simulations is only to provide supplementary explanations to the experimental results, without performing further parametric numerical studies to predict any phenomenon or regime boundary. In the following, the simulations (summarized in Table II) are compared to the experimental images to ensure that the primary experimental phenomena are well reproduced, and the validity of the axisymmetric computation is substantiated. According to the validation of the numerical method shown in Appendix B, a grid resolution of $D_0/\xi = 80$ can adequately capture the deformation and breakup of the interface and the mixing pattern in the pool. Therefore, the following simulations of long-time mixing (Cases 1–3 and 7–9) utilize such a grid resolution of $D_0/\xi = 80$, while a more refined grid resolution of $D_0/\xi = 160$ is employed in the simulations of short-time

dynamics of the first breakup (Cases 4–6). For all the cases, the numerical interface *Pèclet* number $\mathrm{Pe}_i = \xi\sqrt{\sigma_\mathrm{d}/(\rho_\mathrm{d}R_0)}/(M_0\beta_0)$ is fixed at 1.16 to keep the liquid-gas interface close to the equilibrium profile throughout the droplet impact process. Time is normalized by $t^* = (t - t_0)/t_\mathrm{osc}$, where t_0 denotes the onset of coalescence, and $t_\mathrm{osc}=\sqrt{\rho R_0^3/\sigma_\mathrm{d}}$ is the oscillation time of the droplet.

III. RESULTS AND DISCUSSION

Figure 2 shows the typical phenomena observed in the experiments of a water droplet impacts on an ethanol reservoir, including two jet breakups of the liquid-gas interface and strong vortical mixing in the reservoir. Specifically, the first breakup occurs shortly upon coalescence, the second breakup occurs after the crater has restored, and the vortical mixing pattern forms gradually during crater formation and restoration. In the following, these three typical phenomena will be separately discussed to clarify the Marangoni effect on the droplet impact process.

A. First breakup during impact crater formation

Compared to droplet impact on a liquid surface of identical fluid, the occurrence of the first breakup is unique in the presence of surface tension difference. This is caused by the "climbing" Marangoni flow along the droplet surface, which entrains abundant fluid upwards and generates a vertical "stretching" effect. In previous studies on droplet coalescence with a negligible impact velocity, such Marangoni effect was found to result in partial coalescence and even intensive droplet ejection [21], which mechanistically corresponds to the first breakup observed in the present study. Therefore, we further conducted experiments in a wide range of $(1 - \sigma^*)$ and We_d to clarify the effect of impact inertia on the occurrence of first breakup. As shown in Fig. 3, the occurrence of the first breakup shows strong dependency on the impact inertia. Specifically, with the increase of We_d, the first breakup transits from "absence" to "presence" and to "absence" at a medium $(1 - \sigma^*)$ [see Fig. 3(a)] and from "presence" to "absence" at a large $(1 - \sigma^*)$ [see Fig. 3(b)]. This indicates that the effect of impact inertia on the interfacial Marangoni flow is positive at a low We_d and negative at a high We_d.

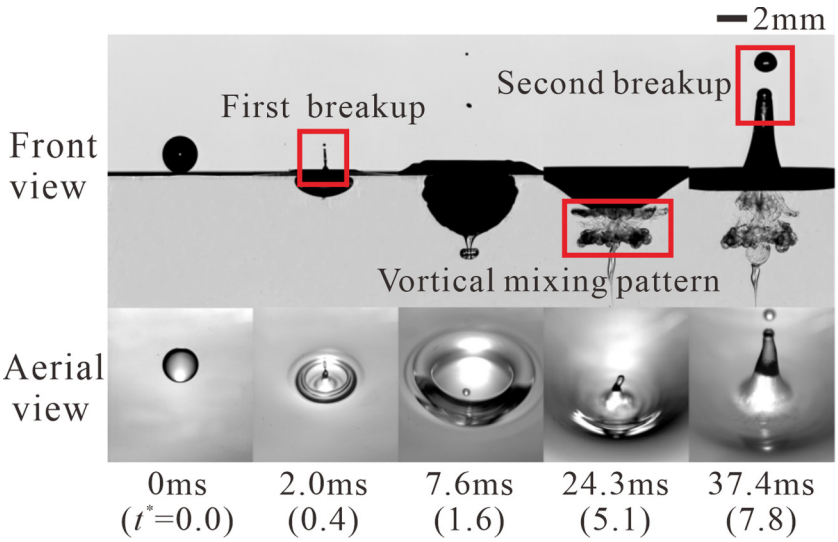

FIG. 2. Typical phenomena during a droplet impacts on a pool of lower surface tension [$\mathrm{We}_\mathrm{d} = 55.6$, $(1 - \sigma^*) = 0.7$].

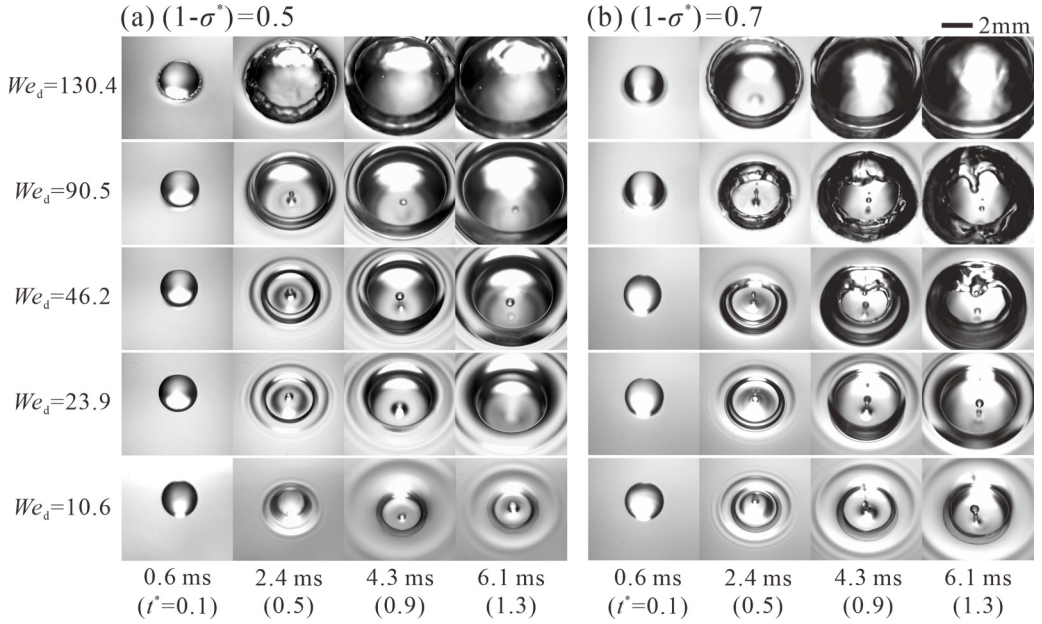

FIG. 3. Nonmonotonic emergence of the first breakup with increasing $\mathrm{We_d}$: (a) $(1-\sigma^*)=0.5$ the first breakup shows a trend of "absence-presence-absence"; (b) $(1-\sigma^*)=0.7$, the first breakup shows a trend of "presence-absence."

To understand these two contradicting effects, we simulated the droplet impact process at three representative $\mathrm{We_d}$ of 20, 90, and 120 and a fixed $(1-\sigma^*)=0.5$, and successfully reproduced the abovementioned non-monotonic emergence of the first breakup. As shown in Fig. 4, the interfacial Marangoni flow converges at the droplet apex and forms a protrusion at $t^*=0.5$ for $\mathrm{We_d}=20$, while it emerges earlier at $t^*=0.35$ for $\mathrm{We_d}=90$ and is even absent for $\mathrm{We_d}=120$. By further looking into the time evolution of the interface morphology, the early impact process can be divided into two stages as illustrated in Fig. 5(a): Stage I, a liquid bridge forms upon coalescence and expands radially outward, while the upper interface of the droplet is almost unaffected; Stage II, the radius of the liquid bridge exceeds R_0 and an impact crater forms with the droplet spreading on its surface.

During Stage I, the growth rate of the liquid bridge is governed by both the capillary pressure and the inertia-driven spreading of the fluid. As illustrated in Fig. 5(b), at a larger $\mathrm{We_d}$, the liquid bridge grows faster and the path for the pool liquid to displace the droplet interface (denoted as l) is reduced. Therefore, the Marangoni flow could converge earlier at the droplet apex with a higher momentum, which is favorable for the occurrence of the first breakup. During Stage II, as illustrated in Fig. 5(c), the absolute displacement velocity of the pool liquid on the expanding crater surface u_{dis} can be decomposed into $u_{\mathrm{dis}}=u_{\mathrm{MF}}-u_{\mathrm{c}}$, in which u_{MF} is the inward converging Marangoni flow velocity and u_{c} denotes the outward expanding velocity of the crater. Temporally, thickness of the mixing front of the Marangoni flow d_{s} tends to diffuse due to continuous dilution by the entrained droplet fluid. With the increase of $\mathrm{We_d}$, the enlarged stretch of the expanding crater surface causes d_{s} to further thicken and thereby reduces u_{MF}, while u_{c} is increased meanwhile. As a result, the outward expansion of the crater becomes increasingly capable of counteracting the inward Marangoni flow, and the first jet no longer emerges beyond a certain high $\mathrm{We_d}$.

The above analysis identified two opposite effects of increased impact inertia on the Marangoni flow during Stage I and during Stage II, respectively, which could be the possible cause for the nonmonotonic emergence of the first jet breakup with an increasing $\mathrm{We_d}$. To verify such hypothesis, theoretical analysis is further conducted. For simplicity, we denote the transition from "no first

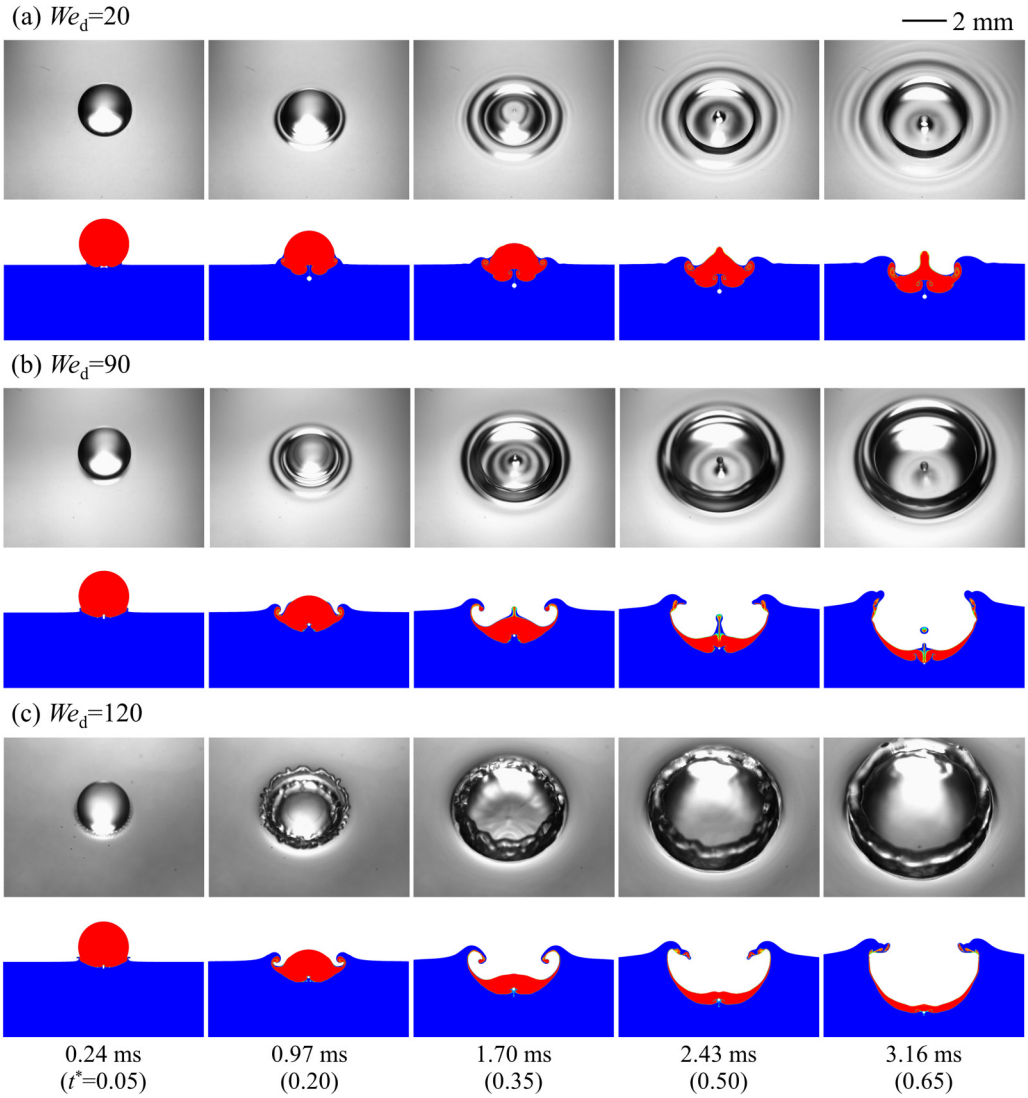

FIG. 4. Simulation of the nonmonotonic emergence of the first breakup at $(1-\sigma^*)=0.5$. The viscosity disparity between the pool (2.4 mPa s) and the droplet (1 mPa s) is not directly included, but alternatively taken into account by using a uniform yet higher Oh = 0.004. The grayscale images are experimental results and the colored images are simulation results.

breakup" to "first breakup" at a small We_d as Boundary 1, and the other transition from "first breakup" to "no first breakup" at a large We_d as Boundary 2. In the following, the characteristic timescales of the crater formation and the Marangoni flow are estimated and compared.

To estimate the timescale for the crater formation, we conceptually simplify the completely formed crater to be an ideal hemisphere with an equivalent radius of R_c and denote the characteristic time for crater formation as t_c. Through balancing the impact inertia ($\sim\rho R_c/t_c^2$) with capillarity ($\sim\sigma_d/R_0^2$), we have $t_c\sim\sqrt{\rho_d R_c R_0^2/\sigma_d}$. At $t=t_c$, the surface energy of the crater $E_c=2\pi R_c^2\sigma_r$ should be comparable with the initial total energy of the system (including the droplet and the

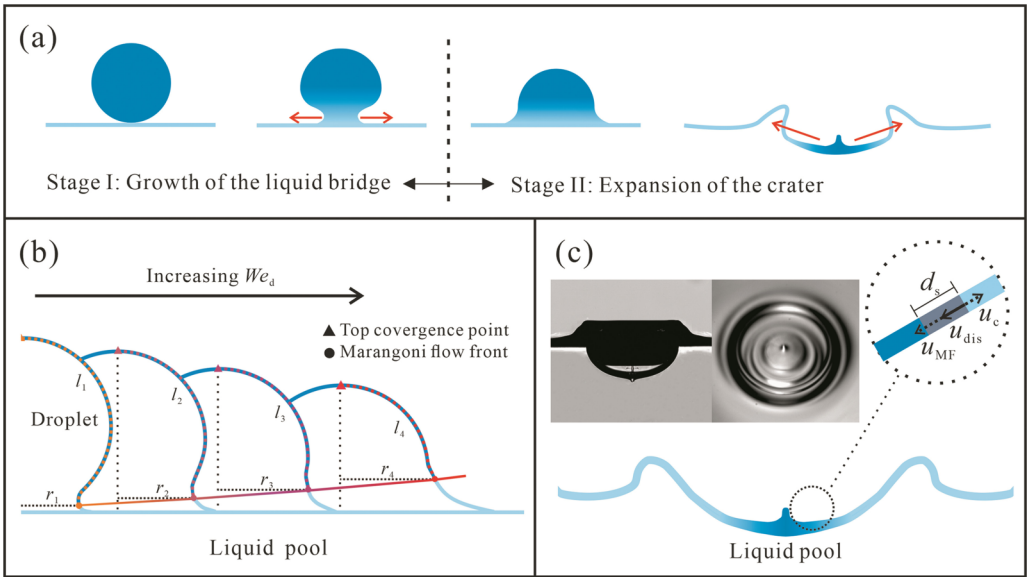

FIG. 5. Schematic of (a) two stages of the droplet impact process; (b) shortened path for the Marangoni flow during Stage I with increasing We_d; (c) decomposition of the absolute displacement velocity on the expanding crater surface during Stage II.

pool of the final crater region) $E_a = 4\pi R_0^2\sigma_d + \pi R_c^2\sigma_r + (2\pi/3)\rho_d R_0^3 U^2$, therefore we have $R_c \sim R_0(We_d/\sigma^*)^{1/2}$ and hence $t_c \sim \sqrt{\rho_d R_0^3/\sigma_d}(We_d/\sigma^*)^{1/4} = t_{osc}(We_d/\sigma^*)^{1/4}$.

To estimate the timescale for the Marangoni flow to displace the droplet surface t_{MF}, we follow the above-mentioned division of the impact process, i.e., t_{MF1} denotes the time for the liquid bridge radius r_b to reach R_0 during Stage I, and t_{MF2} denotes the time for the Marangoni flow to propagate on the crater surface during Stage II. For both situations, we assume a constant Marangoni flow velocity u_{MF}, which can be derived through balancing the Marangoni stress and the viscous stress as $u_{MF} \sim (\delta/R_0)\Delta\sigma/\mu_d$, where δ denotes the fluid layer thickness entrained by the interfacial shear flow. By estimating $\delta \sim \sqrt{\mu_d\sqrt{\rho_d R_0^3/\sigma_d}/\rho_d} \sim R_0\sqrt{Oh}$ [22], u_{MF} can be simplified as $u_{MF} \sim \sqrt{Oh}\Delta\sigma/\mu_d$. For Stage I, by balancing the inertia of the expanding bridge ($\sim \rho_d R_0/t_{MF1}^2$) with capillarity and the increased internal dynamic pressure due to impact [$\sim(\sigma_r/R_0 + \rho_d U^2)/R_0$], t_{MF1} can be estimated as $t_{MF1} \sim t_{osc}/\sqrt{\sigma^* + We_d/2} \sim t_{osc}We_d^{-1/2}$. For Stage II, by considering a limiting case that the Marangoni flow propagates over the entire crater surface of $(\pi/2)R_c$ length, t_{MF2} can be estimated by $t_{MF2} \sim (\pi/2)R_c/u_{MF} \sim R_0\mu_d(We_d/\sigma^*)^{1/2}/[\sqrt{Oh}\sigma_d(1-\sigma^*)]$. Therefore, t_{MF} is finally derived as $t_{MF} \sim t_{MF1} + t_{MF2} \sim t_{osc}We_d^{-1/2} + R_0\mu_d(We_d/\sigma^*)^{1/2}/[Oh^{1/2}\sigma_d(1-\sigma^*)]$.

By comparing these two timescales of the displacement of Marangoni flow on the droplet surface t_{MF} and the formation of the impact crater t_c, we have $t_{MF}/t_c \sim We_d^{-3/4}\sigma^{*1/4} + We_d^{1/4}Oh^{1/2}\sigma^{*-1/4}/(1-\sigma^*) \sim We_d^{-3/4}[1-(1-\sigma^*)]^{1/4} + We_d^{1/4}Oh^{1/2}[1-(1-\sigma^*)]^{-1/4}/(1-\sigma^*)$. With the increase of We_d, $We_d^{-3/4}[1-(1-\sigma^*)]^{1/4}$ decreases while $We_d^{1/4}Oh^{1/2}[1-(1-\sigma^*)]^{-1/4}/(1-\sigma^*)$ increases, which represent the "promotion" and the "suppression" effects on the first breakup at a low We_d and a high We_d, respectively. Therefore, for Boundary 1, the shortened duration of Stage I that represented by $We_d^{-3/4}[1-(1-\sigma^*)]^{1/4}$ is dominant, suggesting the critical We_d for the transition might show a dependence on $[1-(1-\sigma^*)]^{1/3}$. For Boundary 2, the contribution of $We_d^{1/4}Oh^{1/2}[1-(1-\sigma^*)]^{-1/4}/(1-\sigma^*)$ is determinative, indicating a correlation could exist between We_d and $[1-(1-\sigma^*)](1-\sigma^*)^4/Oh^2$.

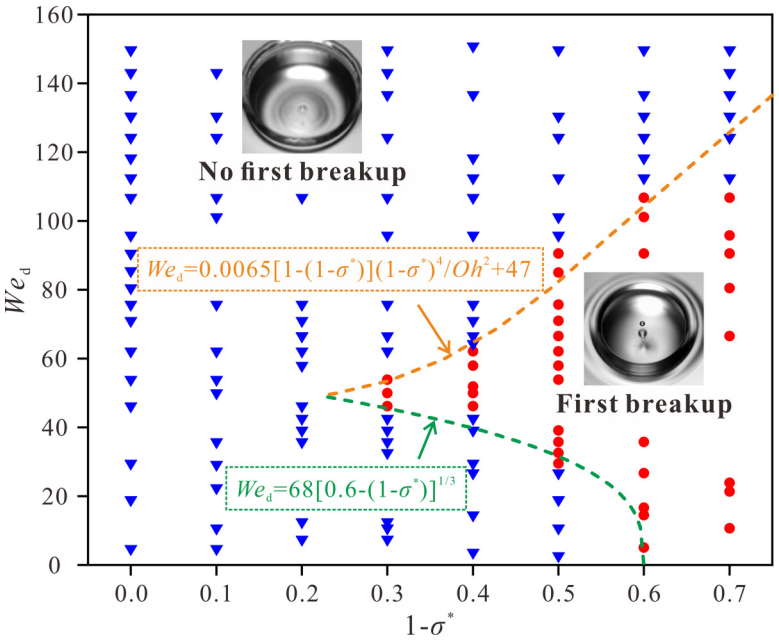

FIG. 6. Experimental regime diagram for the first breakup. The green dotted line indicates the transition from "absence" to "presence" of the first breakup at a small $\mathrm{We_d}$, and the black dotted line indicates the transition from "presence" to "absence" of the first breakup at a large $\mathrm{We_d}$.

To verify these two hypotheses, we further plot all the experimental outcomes in the regime diagram of Fig. 6, and readily find that Boundary 1 agrees well with $\mathrm{We_d} = 68[0.6 - (1-\sigma^*)]^{1/3}$, and Boundary 2 agrees well with $\mathrm{We_d} = 0.0065[1-(1-\sigma^*)](1-\sigma^*)^4/\mathrm{Oh}^2 + 47$. The shift of Boundary 1 towards a smaller $(1-\sigma^*)$ (i.e., the appearance of $[0.6-(1-\sigma^*)]^{1/3}$ instead of $[1-(1-\sigma^*)]^{1/3}$ is caused by the fact that, for the limiting situation of droplet coalescence with negligible impact inertia, the first breakup depends on the competition between the upward Marangoni flow and the downward retraction of droplet towards the pool and occurs as long as $(1-\sigma^*)/\sqrt{\mathrm{Oh}} > 6.75$ [22], which is not included in the above analysis. The shift of Boundary 2 towards a larger $\mathrm{We_d}$ (i.e., the appearance of "+47") originates from the shortened Stage I that is represented in $\mathrm{We_d^{-3/4}}[1-(1-\sigma^*)]^{1/4}$. The overprediction of the Boundary 2 at $(1-\sigma^*) = 0.7$ is because of that we assume a constant Marangoni flow velocity, which cannot represent the increasingly prominent dilution of the mixing front of the Marangoni flow on the expanding crater interface at an extremely large $\mathrm{We_d}$.

B. Second breakup during crater restoration

Figure 7 shows the droplet impact process at different $\mathrm{We_d}$ and two $(1-\sigma^*)$ of 0.4 and 0.6. The second breakup occurs monotonically beyond a certain $\mathrm{We_d}$, and both singular jet and cavity jet were identified. This indicates that, the second breakup for $(1-\sigma^*) > 0$ corresponds to the Rayleigh jet breakup for $(1-\sigma^*) = 0$, which is caused by the pinch-off of the liquid column by Rayleigh-Plateau instability. Moreover, by comparing the two cases at $\mathrm{We_d} = 70$, it is also found that the critical $\mathrm{We_d}$ for the second breakup decreases with $(1-\sigma^*)$, as the second breakup is absent for $(1-\sigma^*) = 0.4$ but is present for $(1-\sigma^*) = 0.6$. Therefore, we plot all the experimental results in the $\mathrm{We_d}$ vs $(1-\sigma^*)$ regime diagram of Fig. 8(a), and surprisingly find that the critical $\mathrm{We_d}$ decreases linearly with $(1-\sigma^*)$.

It is noted that, by using ethanol-water mixture as the pool liquid, μ_r may increase to over twice μ_d at medium $(1-\sigma^*)$ and therefore enlarges the effective Oh number. However, since the

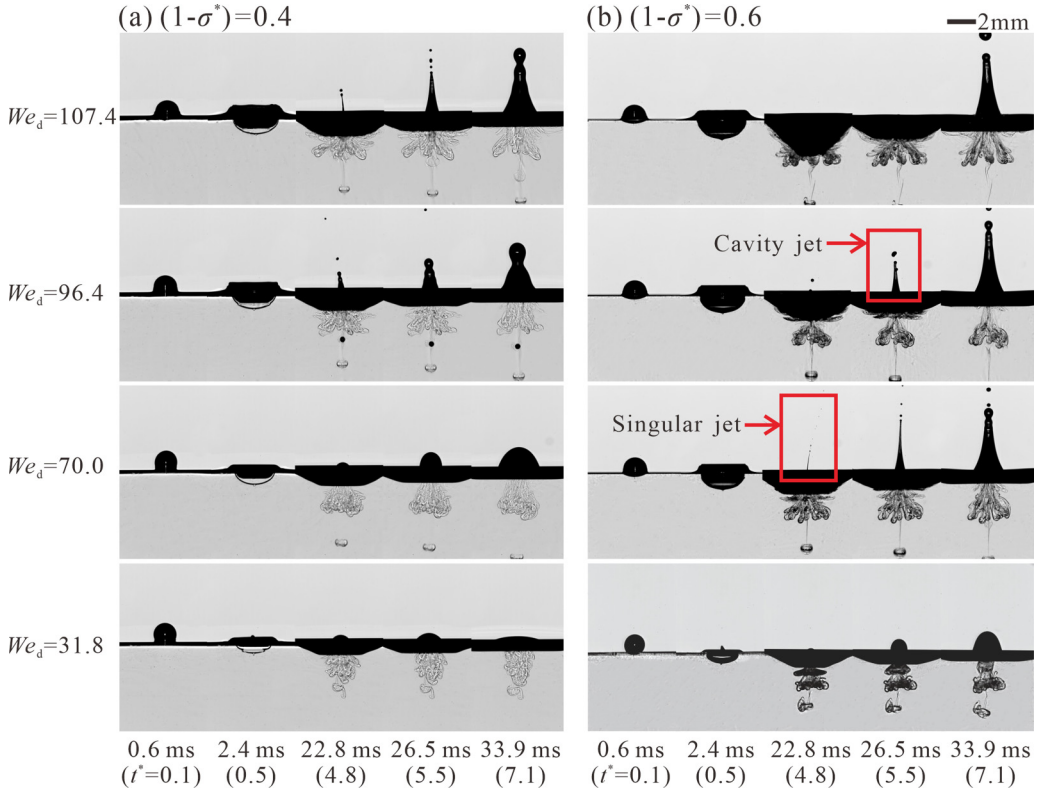

FIG. 7. Experimental results on the second breakup: (a) $(1-\sigma^*)=0.4$, (b) $(1-\sigma^*)=0.6$. For both cases, the second breakup occurs beyond a certain $\mathrm{We_d}$.

formation and retraction of the crater can be viewed as a large-wavelength, low-frequency oscillation of the interface, its breakup dynamics is insignificantly affected by the viscous effect [40]. This indicates that the decrease of critical $\mathrm{We_d}$ with $(1-\sigma^*)$ is not affected by the unavoidable variation of μ_r but dominated by the surface tension of the interface.

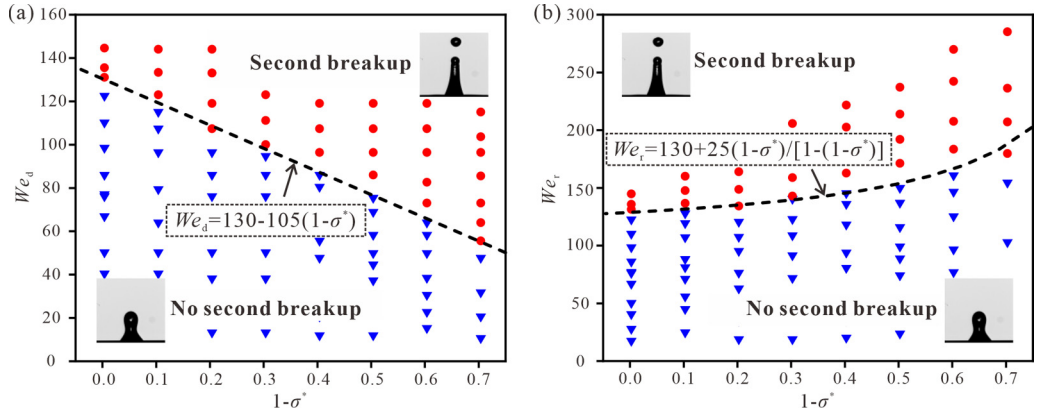

FIG. 8. Experimental regime diagram of the second breakup in the coordinate system of (a) $\mathrm{We_d}$ vs $(1-\sigma^*)$ and (b) $\mathrm{We_r}$ vs $(1-\sigma^*)$.

We also note that the effect of gravity is critical on the crater collapse, and thus affects the critical We_d for the emergence of the second jet breakup. For droplet impacts onto a pool of same fluid with $(1-\sigma^*)$, such effect has been widely studied in literature. It was found that gravity exhibits rather complex influences on the singularity formation, bubble entrainment and crater restoration by affecting the growth of crater and the propagation of the surface waves [41–49]. At maximum crater deformation, the gravitational potential energy may even take up most of the crater energy, which will be subsequently transformed into the energy of the central jet including the kinetic energy required for jet breakup [49–51]. In the present study with a fixed $Bo = 0.75$, the role of gravity is implicitly included in the critical We_d number at $(1-\sigma^*) = 0$, which is identified to be $We_{d0} = 130$ and agrees well with the results by Rein *et al.* [43] and Michon *et al.* [49]. On this basis, the focus of the present study is to further clarify the Marangoni effect on the critical We_d at $(1-\sigma^*) > 0$ under a fixed Bo.

In this regard, recall that the relative displacement time of the Marangoni flow on the expanding crater surface was estimated by $t_{MF}/t_c \sim We_d^{-3/4}[1-(1-\sigma^*)]^{1/4} + We_d^{1/4}Oh^{1/2}[1-(1-\sigma^*)]^{-1/4}/(1-\sigma^*)$, which is smaller than unity for most experimental cases with the second breakup. This indicates that the Marangoni flow has converged at central crater surface before the crater reaches maximum deformation, and σ_r should govern the capillary force of the impact crater. As such, we redefined another We number based on σ_r as $We_r = \rho_d U^2 D_0/\sigma_r$, and replotted the experimental outcomes in Fig. 9(b). As shown in the figure, the critical We_r increases with $(1-\sigma^*)$, which could be caused by the increased viscous dissipation from the Marangoni flow. This is because that the utilization of We_r conceptually corresponds to an idealized situation that the droplet surface is instantaneously wrapped up by the pool liquid upon coalescence, while in reality the Marangoni-flow-induced viscous dissipation during the finite-time "wrap up" process consumes additional kinetic energy.

To derive such increased viscous dissipation energy E_d induced by the Marangoni flow, we estimate the viscous dissipation rate by $\Phi \sim \mu_d(u_{MF}/\delta)^2 \sim \sigma_d^2(1-\sigma^*)^2/(\mu_d R_0^2)$, estimate the volume of the Marangoni flow shear layer as $V_{shear} \sim 2\pi R_c \delta a_1 \sim 2\pi a_1 R_0^3 We_r\sqrt{Oh}$, and estimate the time for the convergence of Marangoni flow as $t_{MF} \sim a_2 t_{MF2} \sim a_2 R_0 \mu_d We_r^{1/2}/[Oh^{1/2}\sigma_d(1-\sigma^*)]$, in which a_1 and a_2 are two coefficients of $O(10^{-1})$ since the Marangoni flow converges early before the crater completely forms. It is also noted that t_{MF1} is not included in estimating t_{MF} since the second breakup occurs at a certain large We_d. As such, we have $E_d \sim \Phi V_{shear} t_{MF} \sim a_1 a_2 We_r^{3/2}\sigma_d(1-\sigma^*)R_0^2$.

For the emergence of the second breakup, such excessive E_d is consumed by a certain additional initial kinetic energy, therefore the critical We_r could show a form of $We_r \sim We_{r0} + E_d/(4\pi R_0^2\sigma_r) \sim We_{r0} + a_3 We_{r0}^{3/2}(1-\sigma^*)/[1-(1-\sigma^*)]$, in which $We_{r0} = We_{d0} = 130$ is the critical We_r at $(1-\sigma^*) = 0$ and $Bo = 0.75$, and $a_3 We_{r0}^{3/2}(1-\sigma^*)/[1-(1-\sigma^*)]$ represents the additional viscous loss, with a_3 being a coefficient of $O(10^{-3})$. According to the present experimental results, we readily find that the critical condition agrees well with $We_r = 130 + 25(1-\sigma^*)/[1-(1-\sigma^*)]$, which can be equivalently expressed by the abovementioned $We_d = 130 - 105(1-\sigma^*)$. As such, the experimentally identified linear decrease of the critical We_d with $(1-\sigma^*)$ is directly caused by both the reduction of the crater surface tension and the associated viscous dissipation from the Marangoni flow.

C. Vortical mixing beneath the liquid surface

During droplet impact, vorticity is generated on the deformable liquid-gas interface by the baroclinic torque, which then detaches from the interface and forms a vortical mixing pattern. In the presence of surface tension difference, as shown in Fig. 9, vortical mixing is found to be enhanced compared to the situation with $(1-\sigma^*) = 0$. Specifically, at a small We_d (e.g., $We_d = 10$), although a similar mixing pattern of "a central jet with a vortical structure" is formed as in the situation with $(1-\sigma^*) = 0$, the vortical structure appears to be more intensive. With the increase of We_d,

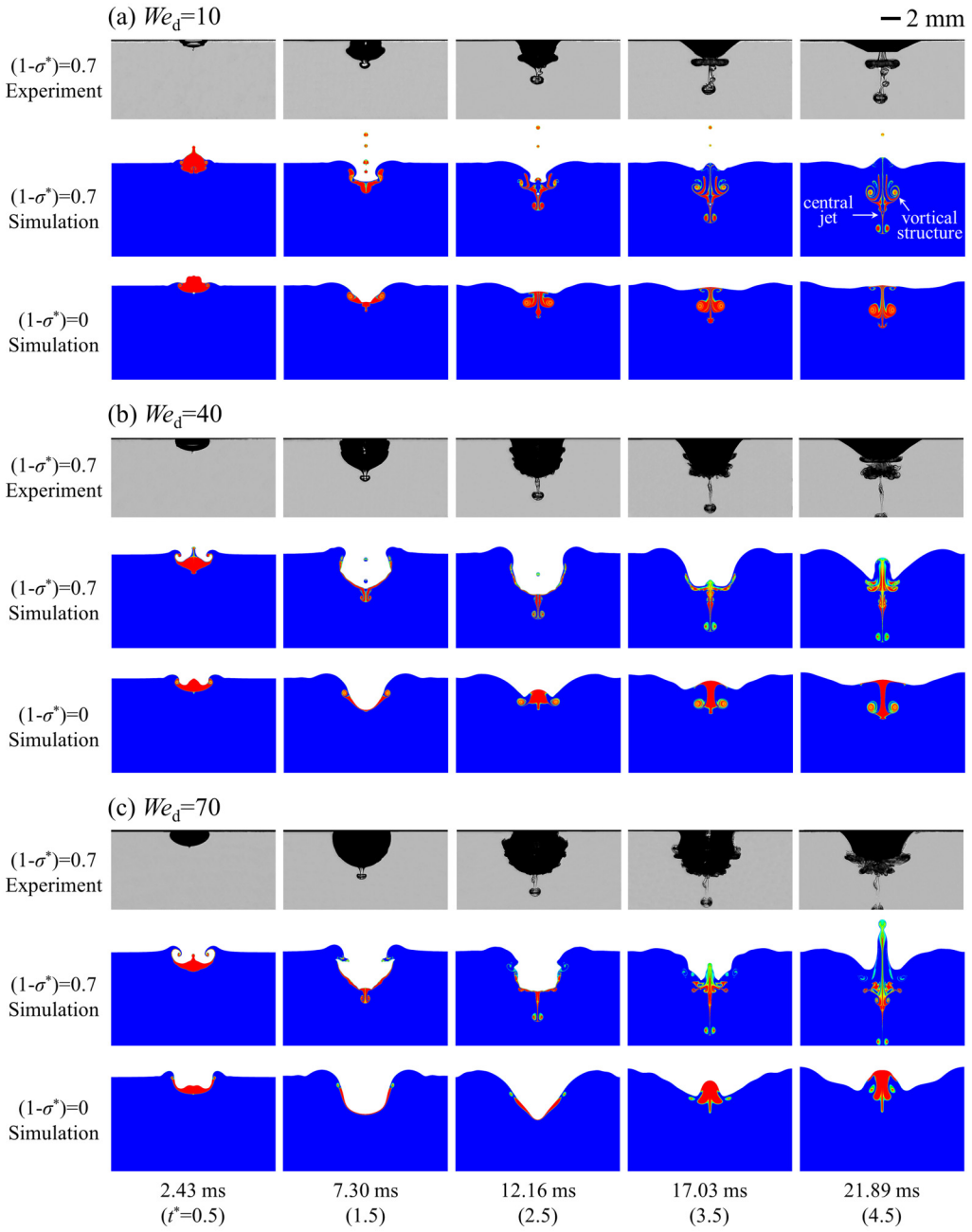

FIG. 9. Vortical mixing beneath the liquid surface: (a) $We_d = 10$, (b) $We_d = 40$, (c) $We_d = 70$. The grayscale images are experimental results and the colored images are simulation results.

multiple layers of vortical structure were observed for $We_d = 40$ and $We_d = 70$. In contrast, the simulations with $(1 - \sigma^*) = 0$ show no enhancement of mixing at enlarged We_d, and the central jet is no longer observed for $We_d = 70$. Figure 10 compares the vorticity fields with the concentration fields at $t^* = 4.5$ for the three cases at $(1 - \sigma^*) = 0.7$, which clearly shows that the vortical mixing

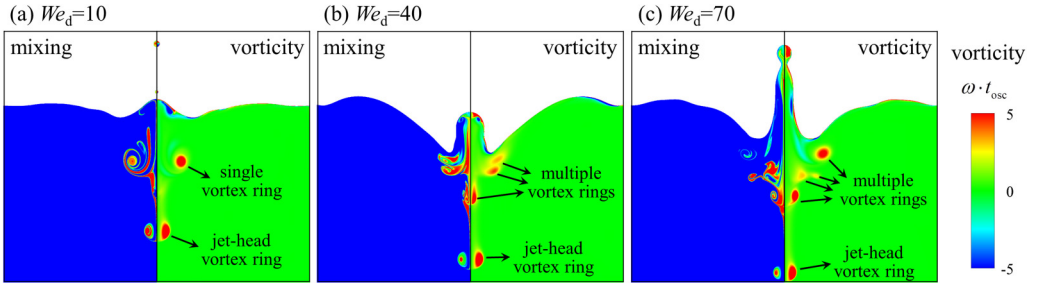

FIG. 10. Comparison of the mixing pattern and the vorticity field at $t^* = 4.5$: (a) $\mathrm{We_d} = 10$, (b) $\mathrm{We_d} = 40$, (c) $\mathrm{We_d} = 70$. $(1 - \sigma^*) = 0.7$ in all three cases.

structures in the concentration field correspond well with the vortex rings in the vorticity field. In addition, most of the vorticity is located in the twin-fluid mixing region instead of in the pure reservoir-fluid region, which could therefore result in enhanced mixing between the droplet and the reservoir.

To explain the enhanced mixing with surface tension difference, we schematically summarize the formation of the vortex rings from numerical simulations in Fig. 11. For simplicity, we follow the definition of two stages of the early impact process used above, i.e., Stage I corresponds to the expansion of the liquid bridge, Stage II denotes the formation of the crater, and we further denominate a Stage III as the restoration of the crater. During Stage I, the rapid expansion of the liquid bridge induces an anticlockwise rotating vortex (vortex 1) in the vicinity of the droplet-side interface, which soon detaches from the interface with negative vorticity generation from interface deformation. For $(1 - \sigma^*) > 0$, however, the interfacial Marangoni flow entrains the interior liquid towards the interface, thus the detached vortex 1 could stay much closer to the interface compared to the case of $(1 - \sigma^*) = 0$. Consequently, during Stage II, deformation of the interface is largely affected by such vortex, whose rotating motion causes the outer crater to form an inward rim for $(1 - \sigma^*) > 0$, while a smooth bowl-shaped crater is formed for $(1 - \sigma^*) = 0$ without much interference from vortex 1.

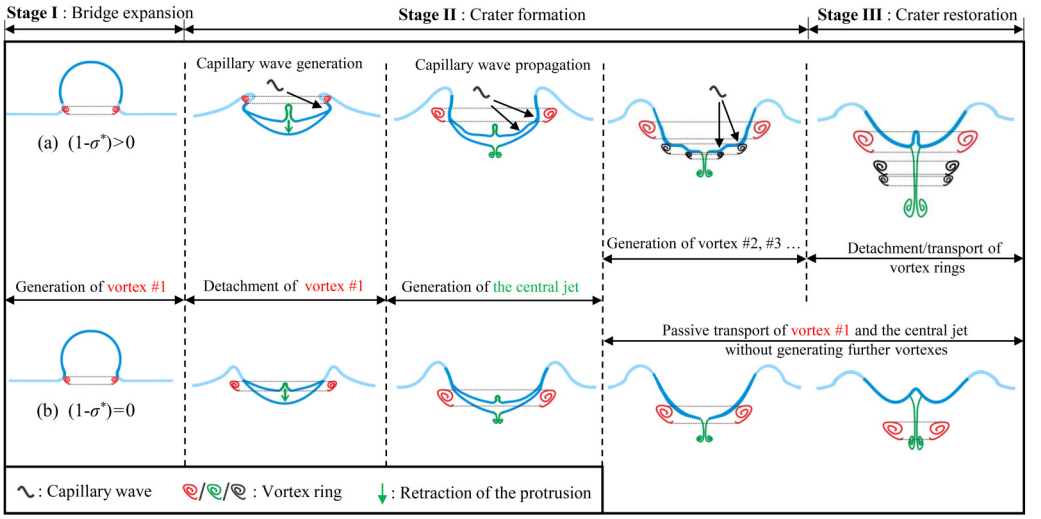

FIG. 11. Comparison of the formation of vortical mixing pattern of (a) with surface tension difference, i.e., $(1 - \sigma^*) > 0$; (b) without surface tension difference, i.e., $(1 - \sigma^*)=0$.

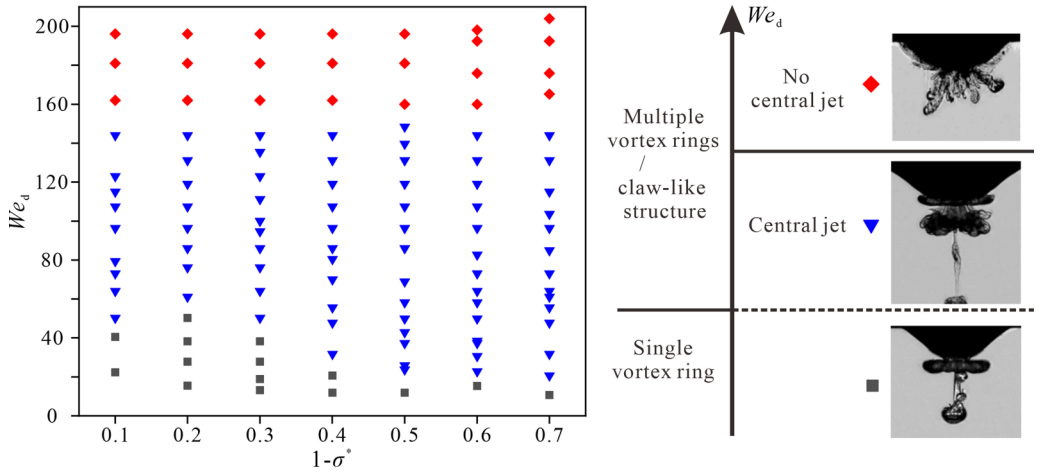

FIG. 12. Experimental regime diagram of the mixing pattern beneath the liquid surface.

Meanwhile, the convergence of Marangoni flow at central crater surface forms a protrusion for $(1-\sigma^*) > 0$, which finally retracts under the capillary pressure gradient and forms the central jet into the pool. For $(1-\sigma^*) = 0$, although a protrusion can also form by the convergence of capillary wave, it appears to be much less sharp in morphology and flattens with the spreading motion of the interface at increased We_d. Therefore, in the presence of surface tension difference, the central jet exhibits a more intensive pattern with a deeper penetration depth and a stronger vortex ring at the head, and such a pattern could be sustained in a much wider range of We_d.

During subsequent crater formation and restoration, i.e., late Stage II and Stage III, the inwardly curved rim retracts under surface tension for $(1-\sigma^*) > 0$, and capillary waves are consequently induced on the crater surface. As the capillary waves propagate towards the crater center, additional vortices are induced on the deformed interface, which then detach from the interface and eventually form multiple vortex rings in the reservoir. For $(1-\sigma^*) = 0$, in contrast, the expansion and restoration of the smooth crater is not accompanied by such capillary waves and associated vorticity generation, and the mixing pattern remains to further evolve a central jet with a single vortex ring.

Having understood the underlying physics of vortical mixing formation, the experimental regime diagram for the mixing pattern is finally presented in Fig. 12. The mixing pattern is characterized from two aspects: (1) the appearance of a central jet and (2) the number of vortex rings. At a large We_d, radial asymmetry becomes prominent and the multiple vortex rings turn into clawlike structures. However, due to the difficulty in clearly identifying the vortical structures from experimental results, we only classify the number of vortex rings into single structrues and multiple or clawlike structures. As shown in the figure, the emergence of more complex vortical mixing pattern is facilitated by enlarging the surface tension difference, which further substantiates the abovementioned critical role of Marangoni flow in facilitating vortical mixing. Moreover, the central jet is absent above a certain large We_d of approximately 160, which also substantiates the negative effect of crater expansion on the converging Marangoni flow during the formation of the central jet.

IV. CONCLUDING REMARKS

In the present study, the impact dynamics and internal mixing of a droplet onto a liquid-gas interface of lower surface tension was studied experimentally by high-speed imaging and numerically by using the lattice Boltzmann phase-field method. Particular attention was paid to three

characteristic phenomena identified in the experiments, including the first breakup during impact crater formation, the second breakup during crater restoration, and the vortical mixing beneath the liquid surface. In the study, Oh and Bo are fixed, and We_d and $(1-\sigma^*)$ are varied as controlling parameters.

The emergence of the first breakup during impact crater formation is unique in the presence of surface tension difference. With the increase of the impact inertia, the first breakup shows a nonmonotonic trend of "absence-presence-absence." Two opposite effects of the impact inertia imposes on the Marangoni flow were identified at a low We_d and a high We_d, respectively. Specifically, at a low We_d, a higher impact inertia shortens the path of the Marangoni flow on the faster growing liquid bridge surface, and the critical condition for the emergence of the first jet was identified to be $We_d = 68(\sigma^* - 0.4)^{1/3}$; at a high We_d, the absolute displacement velocity of the Marangoni flow is largely offset by the expanding motion of the crater surface, and the critical condition for the disappearance of the first breakup was found to be $We_d = 0.0065\sigma^*(1-\sigma^*)^4/Oh^2+47$.

The second breakup corresponds to the Rayleigh jet breakup for $(1-\sigma^*)=0$ and occurs monotonically beyond a certain We_d. Due to the relatively short displacement time of the Marangoni flow on the crater surface compared to the time for crater formation, the critical We_d for the emergence of the second jet breakup was found to be determined by the surface tension of the reservoir fluid and affected by the increased viscous dissipation from the Marangoni flow. The critical condition was theoretically derived and experimentally validated as $We_r = 130 + 25(1-\sigma^*)/[1-(1-\sigma^*)]$ or equivalently a linear dependence of $We_d = 130 - 105(1-\sigma^*)$, in which 130 is the Bo-dependent, critical We number at $(1-\sigma^*)=0$.

Furthermore, Marangoni effect was also found to enhance mixing beneath the liquid surface. At a small We_d, the mixing pattern exhibits a central jet with a single vortex ring, while multiple vortex rings and even clawlike structures were observed at a large We_d. The generation of multiple vortex rings is caused by the propagation of capillary waves on the crater surface. Such capillary waves originate from the restoration of the Marangoni-flow-induced, inwardly curved rim during impact crater formation.

Finally, we note that the results presented in this paper were conducted at fixed Bo and Oh numbers. With other Bo and Oh numbers, the underlying physics of the Marangoni effect on the droplet impact process is believed to be the same, while the exact boundaries for different regimes should vary. A further quantitative study has gone beyond the capability of the present experiments and simulations and merits further studies in future.

ACKNOWLEDGMENTS

This work was financially supported by the National Natural Science Foundation of China (No. 51606134) and the National Natural Science Funds for Distinguished Young Scholar (No. 51525603). The work in the Hong Kong Polytechnic University was partially supported by DGRF (G-UAHP).

APPENDIX A: EXPERIMENTAL ERROR ANALYSIS

Among the four major nondimensional parameters in the present study, $(1-\sigma^*)$ is only related to the preparation of the water-ethanol solutions of different compositions, while We_d, Oh, and Bo involve both physical properties such as density ρ, dynamic viscosity μ, and surface tension σ, as well as the droplet diameter D_0 and the impact velocity U. The physical properties are believed to be accurate, and the errors are therefore mainly originating from D_0 and U.

In the present experiments, the droplet diameter D_0 was fixed at approximately 2.4 mm by using the same needle, and this approximate D_0 was used to calculate the "fixed" Oh and Bo. However, and the exact value of D_0 varied in the range of 2.33–2.40 mm, thereby inducing a relative error $\delta_{D0,1}$ of -2.9% to 0%. In addition, exact measurements of D_0 were done by counting pixels in the

TABLE III. Relative errors of the nondimensional parameters in the experimental results.

Nondimensional parameter	Sources of error	Relative error
$1-\sigma^*=(\sigma_d-\sigma_r)/\sigma_d$	solution preparation	negligible
$We_d=\rho_d U^2 D_0/\sigma_d$	U (recognition of pixels), D_0 (recognition of pixels)	−4.8% to 4.8%
$Oh=\mu_d/\sqrt{\rho_d\sigma_d D_0}$	D_0 (recognition of pixels, variation in the droplet size)	−0.8% to 2.3%
$Bo=(\rho_d-\rho_g)gD_0^2/\sigma_d$	D_0 (recognition of pixels, variation in the droplet size)	−8.8% to 3.2%

camera-recorded images, and recognition of an unsharp droplet morphology may also include an error of ±2 pixels on D_0. Since the average number of pixels to resolve D_0 is 124, this also includes a relative error $\delta_{D0,2}$ of −1.6% to 1.6%. We also note that, in the experimental regime diagrams, We_d was calculated by using exact pixels of each individual experimental case, while Oh and Bo are approximately fixed and estimated by using $D_0 \approx 2.40$ mm. Therefore, both $\delta_{D0,1}$ and $\delta_{D0,2}$ (totally −4.5% to 1.6%) were included in estimating Oh and Bo, while only $\delta_{D0,2}$ (totally −1.6% to 1.6%) was included in determining We_d.

Moreover, the impact velocity U was determined by counting the number of pixels of the droplet center (an average coordinate of the lower and the upper interface) moved within the last two frames prior to impact (at a constant frame rate of 5400 fps). Therefore, an error of ±2 pixels in recognizing the droplet displacement could be also involved, yielding a relative error δ_{U0} of −1.6% to 1.6%.

In view of above, the errors for We_d, Oh, and Bo are further calculated based on their dependences on D_0 and U, which are given in Table III.

APPENDIX B: NUMERICAL VALIDATION

Case 1 in Table II [$We_d = 10$, $Oh = 0.0022$, $(1-\sigma^*) = 0.7$] was employed to validate the numerical method. Figure 13 compares the experimental result with simulations by using different grid resolutions. In the simulations, the interface thickness ξ is consistently resolved by five grid points, and the droplet diameter D_0 is resolved by 250–450 grids, corresponding to an increased grid resolution from $D_0/\xi = 50$ to $D_0/\xi = 90$. As shown in the figure, both the first jet breakup of the liquid-gas interface and the vortical mixing pattern in the pool can be adequately captured by using a grid resolution of $D_0/\xi = 80$. A further refined grid of $D_0/\xi = 90$ only leads to slightly different temporal evolution of the mixing pattern.

Regarding the conservations of energy and mass during the droplet impact simulations, we further note that the impact velocities in our experiments were determined from the two sequential images before impact occurs, and accordingly in the simulations the droplet was initially placed above the interface with a short distance of $1/8D_0$. During the free fall, losses in both the energy and the mass are less than 0.1%. Upon impact ($t^* = 0$), the evolution of the normalized total energy (i.e., the sum of kinetic energy, cumulative dissipation energy, surface energy, and gravitational energy) and the normalized droplet liquid mass, with normalization being made by their values at initial condition, are plotted in Fig. 14, and their exact values at $t^* = 4$ are given in Table IV. It is seen that, by using a grid resolution of $D_0/\xi = 80$, the total energy conserves over 95%, and the mass of the droplet liquid conserves over 99% throughout the simulation. In view of the above, a minimum grid resolution of $D_0/\xi = 80$ was used in the present study.

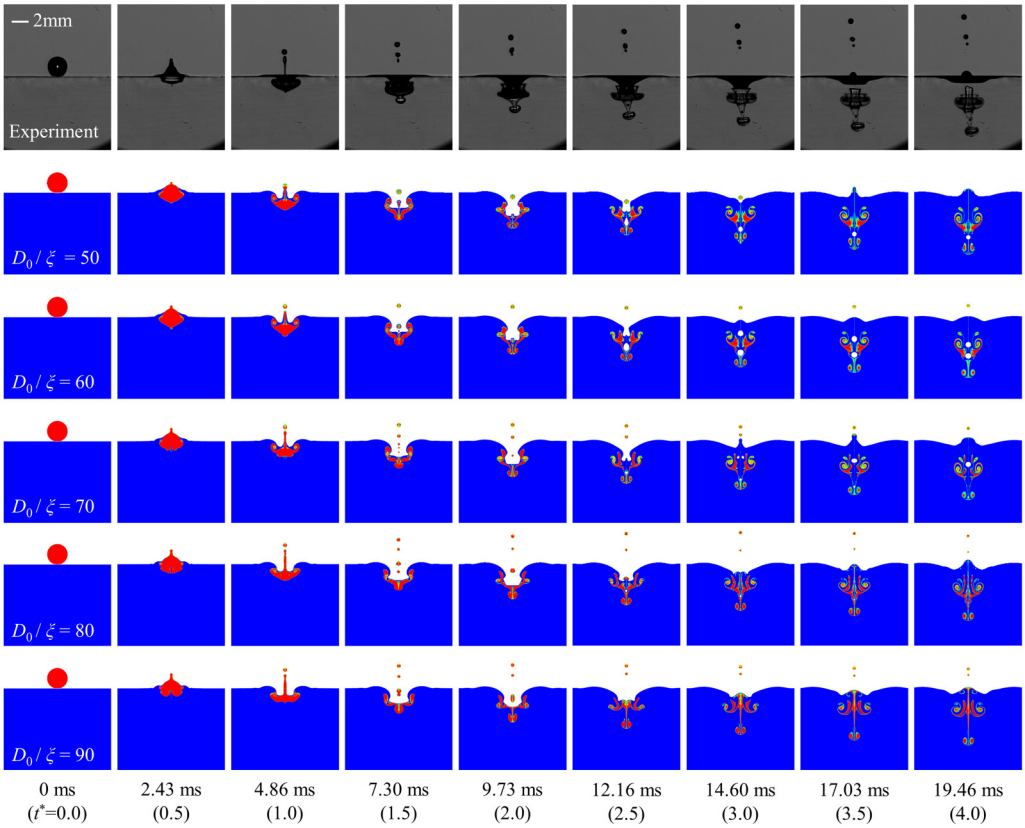

FIG. 13. Experimental validation of the simulations with different grid resolutions [$\mathrm{We_d} = 10$, $\mathrm{Oh} = 0.0022$, $(1-\sigma^*) = 0.7$].

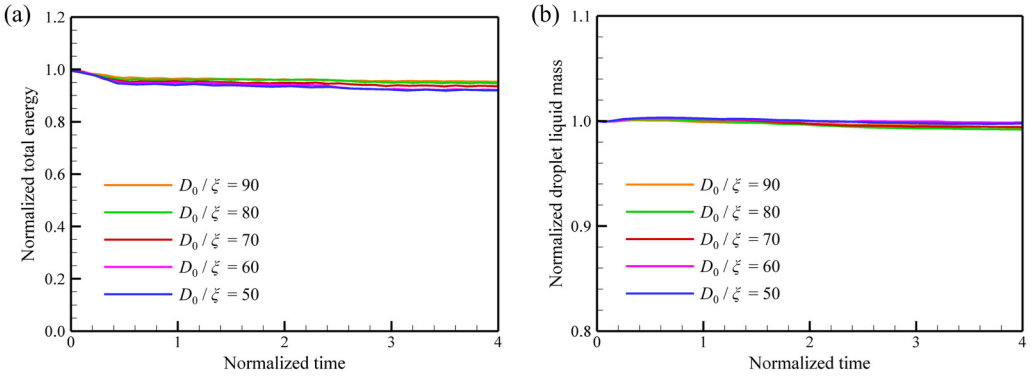

FIG. 14. Conservation of (a) normalized total energy and (b) normalized droplet liquid mass during the simulations with different grid resolutions [$\mathrm{We_d} = 10$, $\mathrm{Oh} = 0.0022$, $(1-\sigma^*) = 0.7$].

TABLE IV. Normalized total energy and normalized droplet liquid mass at $t^* = 4$ [$\mathrm{We_d} = 10$, $\mathrm{Oh} = 0.0022$, $(1 - \sigma^*) = 0.7$].

Grid resolution	Normalized total energy	Normalized droplet liquid mass
$D_0/\xi = 50$	0.9253	0.9975
$D_0/\xi = 60$	0.9233	0.9987
$D_0/\xi = 70$	0.9403	0.9942
$D_0/\xi = 80$	0.9501	0.9918
$D_0/\xi = 90$	0.9562	0.9937

[1] F. Raes, R. V. Dingenen, E. Vignati, J. Wilson, J. Putaud, J. H. Seinfeld, and P. Adams, Formation and cycling of aerosols in the global troposphere, Atmos. Environ. **34**, 4215 (2000).

[2] C. Baumgarten, *Mixture Formation in Internal Combustion Engines* (Springer, Berlin, 2006).

[3] J. Kim, Spray cooling heat transfer: The state of the art, Int. J. Heat Fluid Flow **28**, 753 (2007).

[4] K. L. Pan and C. K. Law, Dynamics of droplet-film collision, J. Fluid Mech. **587**, 1 (2007).

[5] A. L. Yarin, DROP IMPACT DYNAMICS: Splashing, Spreading, Receding, Bouncing …, Annu. Rev. Fluid Mech. **38**, 159 (2006).

[6] E. Castillo-Orozco, A. Davanlou, P. K. Choudhury, and R. Kumar, Droplet impact on deep liquid pools: Rayleigh jet to formation of secondary droplets, Phys. Rev. E **92**, 053022 (2015).

[7] J. R. Castrejón-Pita, B. N. Muñoz-Sánchez, I. M. Hutchings, and A. A. Castrejón-Pita, Droplet impact onto moving liquids, J. Fluid Mech. **809**, 716 (2016).

[8] G. Agbaglah, M. J. Thoraval, S. T. Thoroddsen, L. V. Zhang, K. Fezzaa, and R. D. Deegan, Drop impact into a deep pool: vortex shedding and jet formation, J. Fluid Mech. **764**, R1 (2015).

[9] A. V. Anilkumar, C. P. Lee, and T. G. Tang, Surface-tension-induced mixing following coalescence of initially stationary drops, Phys. Fluids A **3**, 2587 (1991).

[10] A. Saha, Y. Wei, X. Tang, and C. K. Law, Kinematics of vortex ring generated by a drop upon impacting a liquid pool, J. Fluid Mech. **875**, 842 (2019).

[11] H. A. Stone, A. D. Stroock, and A. Ajdari, Engineering flows in small devices: Microfluidics toward a lab-on-a-chip, Annu. Rev. Fluid Mech. **36**, 381 (2004).

[12] D. Velev, B. G. Prevo, and K. H. Bhatt, On-chip manipulation of free droplets, Nature (London) **426**, 515 (2003).

[13] A. M. Nightingale, T. W. Phillips, J. H. Bannock, and J. C. de Mello, Controlled multistep synthesis in a three-phase droplet reactor, Nat. Commun. **5**, 3777 (2014).

[14] A. B. Theberge, E. Mayot, A. E. Harrak, F. Kleinschmidt, W. T. S. Huck, and A. D. Griffiths, Microfluidic platform for combinatorial synthesis in picolitre droplets, Lab Chip **12**, 1320 (2012).

[15] C. K. Law, Fuel options for next-generation chemical propulsion, AIAA J. **50**, 19 (2012).

[16] D. Zhang, P. Zhang, Y. Yuan, and T. Zhang, Hypergolic ignition by head-on collision of N,N,N′,N′-tetramethylethylenediamine and white fuming nitric acid droplets, Combust. Flame **173**, 276 (2016).

[17] E. Li, D. Beilharz, and S. T. Thoroddsen, Vortex-induced buckling of a viscous drop impacting a pool, Phys. Rev. Fluids **2**, 073602 (2017).

[18] S. Thoroddsen, M. Thoraval, K. Takehara, and T. Etoh, Micro-bubble morphologies following drop impacts onto a pool surface, J. Fluid Mech. **708**, 469 (2012).

[19] D. Beilharz, A. Guyon, E. Li, M. Thoraval, and S. Thoroddsen, Antibubbles and fine cylindrical sheets of air, J. Fluid Mech. **779**, 87 (2015).

[20] F. Marcotte, G. J. Michon, T. Séon, and C. Josserand, Ejecta, Corolla, and Splashes from Drop Impacts on Viscous Fluids, Phys. Rev. Lett. **122**, 014501 (2019).

[21] F. Blanchette, L. Messio, and J. W. M. Bush, The influence of surface tension gradients on drop coalescence, Phys. Fluids **21**, 072107 (2009).

[22] K. Sun, P. Zhang, Z. Che, and T. Wang, Marangoni-flow-induced partial coalescence of a droplet on a liquid/air interface, Phys. Rev. Fluids **3**, 023602 (2018).
[23] D. W. Martin and F. Blanchette, Simulations of surfactant effects on the dynamics of coalescing drops and bubbles, Phys. Fluids **27**, 012103 (2015).
[24] H. Kim, J. Lee, T. H. Kim, and H. Y. Kim, Spontaneous Marangoni mixing of miscible liquids at a liquid-liquid-air contact line, Langmuir **31**, 8726 (2015).
[25] F. Blanchette, Simulation of Mixing within Drops due to Surface Tension Variations, Phys. Rev. Lett. **105**, 074501 (2010).
[26] D. Jacqmin, Calculation of two-phase Navier-Stokes flows using phase-field modeling, J. Comput. Phys. **155**, 96 (1999).
[27] P. Yue, J. J. Feng, C. Liu, and J. Shen, A diffuse-interface method for simulating two-phase flows of complex fluids, J. Fluid Mech. **515**, 293 (2004).
[28] T. Lee and L. Liu, Lattice Boltzmann simulations of micronscale drop impact on dry surfaces, J. Comput. Phys. **229**, 8045 (2010).
[29] R. Benzi, S. Succi, and M. Vergassola, The lattice Boltzmann equation: theory and applications, Phys. Rep. **222**, 145 (1992).
[30] Q. Li, K. Luo, and Q. Kang, Lattice Boltzmann methods for multiphase flow and phase-change heat transfer, Prog. Energ. Combust. **52**, 62 (2016).
[31] T. Lee, Effects of incompressibility on the elimination of parasitic currents in the lattice Boltzmann equation method for binary fluids, Comput. Math. Appl. **58**, 987 (2009).
[32] Q. Li, K. H. Luo, and X. Li, Lattice Boltzmann modeling of multiphase flows at large density ratio with an improved pseudopotential model, Phys. Rev. E **87**, 053301 (2013).
[33] Q. Li and K. Luo, Achieving tunable surface tension in the pseudopotential lattice Boltzmann modeling of multiphase flows, Phys. Rev. E **88**, 053307 (2013).
[34] D. Lycett-Brown and K. Luo, Improved forcing scheme in pseudopotential lattice Boltzmann methods for multiphase flow at arbitrarily high density ratios, Phys. Rev. E **91**, 023305 (2015).
[35] D. Lycett-Brown and K. Luo, Cascaded lattice Boltzmann method with improved forcing scheme for large-density-ratio multiphase flow at high Reynolds and Weber numbers, Phys. Rev. E **94**, 053313 (2016).
[36] D. D'Humières, I. Ginzburg, M. Krafczyk, P. Lallemand, and L. Luo, Multiple-relaxation-time lattice Boltzmann models in three dimensions, Philos. Trans. R. Soc. London A **360**, 437 (2002).
[37] K. Sun, M. Jia, and T. Wang, Numerical investigation on the head-on collision between unequal-sized droplets with multiple-relaxation-time lattice Boltzmann model, Int. J. Heat Mass Transfer **70**, 629 (2014).
[38] S. Gottlieb and C. Shu, Total variation diminishing Runge-Kutta schemes, Math. Comput. **67**, 73 (1998).
[39] G. Jiang and C. Shu, Efficient implementation of weighted ENO schemes, J. Comput. Phys. **126**, 202 (1996).
[40] F. Denner, Frequency dispersion of small-amplitude capillary waves in viscous fluids, Phys. Rev. E **94**, 023110 (2016).
[41] H. Oguz and A. Prosperetti, Bubble entrainment by the impact of drops on liquid surfaces, J. Fluid Mech. **219**, 143 (1990).
[42] M. Rein, Phenomena of liquid drop impact on solid and liquid surfaces, Fluid Dyn. Res. **12**, 61 (1993).
[43] M. Rein, The transitional regime between coalescing and splashing drops, J. Fluid Mech. **306**, 145 (1996).
[44] D. Morton, M. Rudman, and L. Jong, An investigation of the flow regimes resulting from splashing drops, Phys. Fluids **12**, 747 (2000).
[45] M. Brenner, Jets from a singular surface, Nature (London) **403**, 377 (2000).
[46] B. Ray, G. Biswas, and A. Sharma, Bubble pinch-off and scaling during liquid drop impact on liquid pool, Phys. Fluids **24**, 082108 (2000).
[47] E. Ghabache, A. Antkowiak, C. Josserand, and T. Séon, On the physics of fizziness: How bubble bursting controls droplets ejection, Phys. Fluids **26**, 121701 (2014).
[48] B. Ray and G. Biswas, and A. Sharma, Regimes during liquid drop impact on a liquid pool, J. Fluid Mech. **768**, 492 (2015).
[49] G. Michon, C. Josserand, and T. Séon, Jet dynamics post drop impact on a deep pool, Phys. Rev. Fluids **2**, 023601 (2017).

[50] A. Ogawa, K. Utsuno, M. Mutou, S. Kouzen, Y. Shimotake, and Y. Satou, Morphological study of cavity and Worthington jet formations for Newtonian and non-Newtonian liquids, Part. Sci. Technol. **24**, 181 (2006).

[51] K. Hasegawa and T. Nara, Energy conservation during single droplet impact on deep liquid pool and jet formation, AIP Adv. **9**, 085218 (2019).